

Purely-long-range krypton molecules in singly and doubly excited binding potentials

Z. S. Smith, A. Harmon, J. Banister, R. Norman, K. Hoogeboom-Pot, and M. Walhout*

Department of Physics and Astronomy, Calvin College, Grand Rapids, Michigan 49546, USA

(Received 20 October 2009; published 14 January 2010)

Diatomic potentials for krypton are computed and also probed experimentally. For a probe-laser wavelength near 811 nm, several strong dipole-dipole interactions produce purely-long-range potential wells in the singly excited manifold of $(s + p)$ potentials and in the doubly excited manifold of $(p + p)$ and $(s + d)$ potentials. Evidence of resonant photoassociation into bound states of these potential wells is observed in the emission of ions and ultraviolet photons from a magneto-optically trapped krypton cloud.

DOI: [10.1103/PhysRevA.81.013407](https://doi.org/10.1103/PhysRevA.81.013407)

PACS number(s): 34.50.Rk

I. INTRODUCTION

In this paper we present preliminary computational and experimental characterizations of diatomic krypton molecules in bound states of purely-long-range (PLR) potential wells. Our calculations reproduce the “singly excited” manifold of $(s + p)$ potentials predicted in Ref. [1]. Among these potentials are 14 PLR potential wells, for which we compute the spectrum of vibrational bound states. We also model the “doubly excited” manifold of $(p + p)$ and $(s + d)$ potentials that may be populated if two atoms in the $1s_5$ pseudo-ground state absorb two probe-laser photons. Within the latter manifold, we identify an unusual class of doubly excited PLR potential wells, which make a notable appearance in the krypton system because several atomic transitions lie close together in energy (see Fig. 1). We use an existing laboratory setup [2] to capture metastable ($1s_5$) krypton atoms in a magneto-optical trap (MOT) and to probe the molecular potentials. Our experimental results are best explained by a combination of photoassociation (PA) processes yielding both singly and doubly excited PLR krypton molecules.

II. DIATOMIC POTENTIALS FOR KRYPTON

As described elsewhere [3], PLR potential wells are usually dominated by the resonant dipole-dipole interaction between atoms in s and p states, and they take on a C_3/R^3 dependence at large internuclear distance (R). The classical inner turning point for the molecular vibration (R_-) is typically a few nm, and the outer turning point (R_+) can approach 100 nm for high-lying states. Among the krypton potentials shown in Fig. 2, several exhibit this PLR character. To compute all of the potentials for this figure, we follow in detail the methods described in Ref. [1], but we use new atomic data [4] as inputs for $(s + p)$ curves, and we expand the set of contributing atomic states in order to produce an appropriate model of the $(p + p)$ and $(s + d)$ manifolds (see Appendix). The authors of Ref. [1] note that the calculation of singly excited potentials is easily separable from that of doubly excited potentials. Since they present only the first calculation, we simply extend their formalism so as to investigate the doubly excited manifold that they ignore. Figure 2(b) shows several singly excited

potentials and agrees very closely with graphs presented in Ref. [1]. Figure 2(a) shows a previously unexamined set of doubly excited potentials, several of which have the form of PLR potential wells. In each case, the PLR character is made apparent by the fact that the classical lower limit for R_- is greater than 1.5 nm.

The PLR potential wells in the upper manifold are the result of a triply resonant dipole-dipole interaction involving the $1s_5 \leftrightarrow 2p_9$, $1s_5 \leftrightarrow 2p_8$, and $2p_9 \leftrightarrow 4d_4'$ atomic transitions. As can be seen in Fig. 2, each PLR minimum is formed from an anticrossing between two potentials—an attractive one that descends from the $(2p_8 + 2p_8)$ asymptote as R decreases, and a repulsive one that rises from the $(1s_5 + 4d_4')$ asymptote. The $|C_3|$ value for the repulsive potential is large, because the $(1s_5 + 4d_4')$ asymptote lies only 16 GHz above the $(2p_8 + 2p_9)$ asymptote. This near-degeneracy leads to a strong dipole-dipole coupling that can be understood in terms of a resonant exchange of photons between atoms. If the system starts on a $(1s_5 + 4d_4')$ potential, the doubly excited atom can emit a photon that the $1s_5$ atom can absorb, so that the system is transferred to a $(2p_8 + 2p_9)$ potential. This process can be reversed, with the $2p_8$ atom decaying and the $2p_9$ atom absorbing the emitted photon. Similar dipole-dipole couplings give rise to the long-range attractive character of the potentials descending from the $(2p_8 + 2p_8)$ asymptote. A “downward push” on these potentials comes mainly from the higher-lying $(1s_5 + 3s_1')$ and $(1s_5 + 4d_4)$ potentials within the doubly excited manifold. Accounting for these interactions allows us to see how the $s - p$ and $p - d$ couplings in the neighborhood of 810 nm conspire to produce doubly excited PLR potential wells.

III. THEORETICAL DISCUSSION

We next address the question of how the production of PLR molecules might lead to measurable effects. To begin, we point out that atoms bound in a PLR well maintain a separation that is always much greater than the size of either atom’s electron distribution. This has an important dynamical consequence: atoms in PLR states are not susceptible to Penning ionization, which is likely only when $R \sim a_0$. Penning ionization normally occurs at a relatively high rate in MOTs for metastable rare-gas atoms, where it is the main density-limiting loss mechanism [5]. Photoassociation of atoms into PLR states can reduce the ionization rate in a trap by maintaining “safe”

*mwalhout@calvin.edu

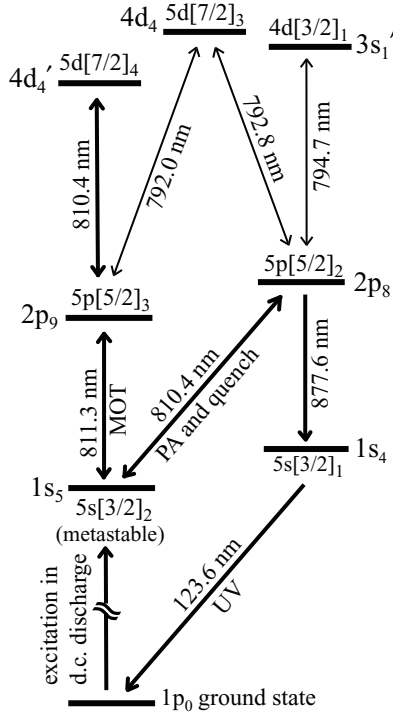


FIG. 1. Some relevant energy levels and transitions in atomic Kr. The values of near-infrared wavelengths are those found in air. Excited atomic states are labeled using both Paschen notation and pair-coupling notation, $n[K = J_c + l]_J$ (in which n is the principal quantum number, J_c is the core's angular momentum, l is the valence electron's orbital angular momentum, and the coupling of K with the valence spin produces the total angular momentum J . l is unprimed if $J_c = 3/2$ and primed if $J_c = 1/2$). Thin arrows represent nonresonant transitions for which there is negligible absorption in our experiment.

distances between atoms for certain kinds of collisions. Our interpretation of experimental ion signals will be based on this effect.

Since there are large $2p_8$ contributions to their electronic wave functions, the bound states in our PLR potential wells will decay at rates comparable to the $2p_8$ spontaneous rate, $\Gamma = 2\pi \times 5$ MHz. The products of this decay may serve as a signature of PA processes. As indicated in the atomic energy level diagram of Fig. 1, the decays will branch into two dominant channels: the $2p_8 \rightarrow 1s_5$ recycling transition (29%) and the $2p_8 \rightarrow 1s_4 \rightarrow 1p_0$ two-step cascade, which ends in the atomic ground state (71%). Both branches may be accompanied by heating and/or loss of atoms in the trap. In addition, each occurrence of the two-step cascade produces two photons, one at wavelength 877.6 nm and another at 123.6 nm. In a trapped Kr cloud exposed to an 810.4-nm laser light, two different processes may lead to the emission of this pair of fluorescence wavelengths. Individual metastable atoms may be “quenched” [2], or pairs of atoms may be photoassociated into PLR states. In the experiments to be described below, we search for molecular resonances in the ultraviolet (UV) fluorescence ($\lambda_{UV} = 123.6$ nm), resonances that can be expected to appear for probe-laser frequencies tuned slightly below the $1s_5-2p_8$ atomic transition.

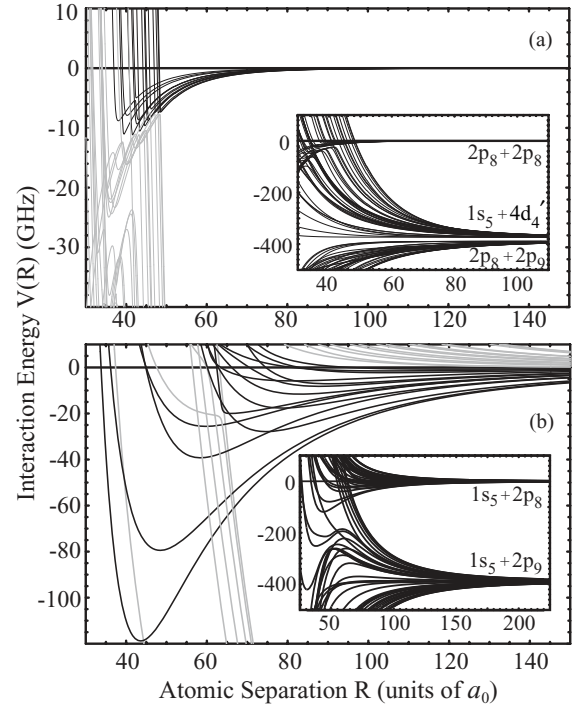


FIG. 2. (a) Doubly and (b) singly excited manifolds of computed diatomic krypton potentials. As discussed in [1], the computation is simplified by the fact that each potential is characterized by a particular value of Ω , the projection of total angular momentum along the internuclear axis. Asymptotes are labeled using pairs of free-atom states in Paschen notation. Potentials with PLR minima (binding potentials) are shown in black; others are shown in gray. Inset boxes: Expanded view of potentials connected to the $(2p_8 + 2p_8)$ and $(1s_5 + 2p_8)$ asymptotes. Atomic separation is given in units of the Bohr radius, $a_0 = 0.053$ nm.

A theoretical, single-photon PA spectrum can be obtained once the vibrational bound-state energies are computed for each PLR $(s + p)$ potential well. We employ a standard numerical algorithm [6] to solve for these energies, finding that the shallowest well in Fig. 2(a) ($V_{\min} = -719$ MHz) supports ten bound states, while the deepest one ($V_{\min} = -118.78$ GHz) supports 62. Given the nested configuration of the potential wells, it is not surprising that the sum of 14 vibrational series produces a complicated overlap of levels near the asymptote. The histogram in Fig. 3 shows the density of states over the 500-MHz range to be addressed in our experiments.

We assume that laser excitation of a PLR $(s + p)$ state will occur at a large Condon radius, $R_+ > 5$ nm, where the $(1s_5 + 1s_5)$ starting energy is very nearly equal to its asymptotic value. We therefore expect the resonance condition for PA transitions to be met when the detuning (Δ) between the laser frequency (ν_L) and the $1s_5-2p_8$ resonance (at ν_0) corresponds to the binding energy (E_b) of a vibrational state: $\Delta \equiv (\nu_L - \nu_0) = E_b/h$, where we assume $E_b < 0$. We can anticipate that an experimental spectrum of resonances will reflect the same pileup and clumping that appears in Fig. 3, though the transition strengths will depend on Franck-Condon factors, saturation effects, sample density, the distribution of initial states, and electric-dipole selection rules.

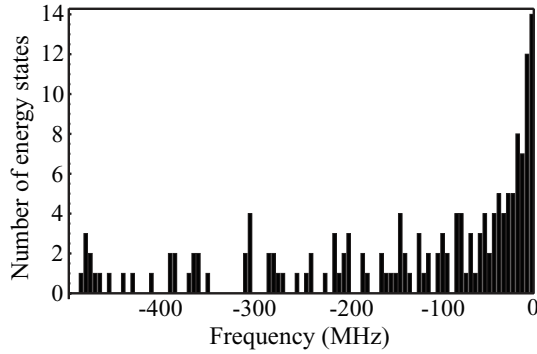


FIG. 3. Density of PLR states lying just below the $(1s_5 + 2p_8)$ asymptote. The vertical axis indicates the number of states that have a binding energy E_b (<0) between E and $(E + h \times 5 \text{ MHz})$.

IV. EXPERIMENTAL PROCEDURES

In our experiments, a dc discharge source generates a beam of metastable Kr atoms, and the method of Zeeman deceleration is used to produce a stream of slow ^{84}Kr atoms for loading our MOT. The trapping beams, which are tuned to the $1s_5-2p_9$ transition at 811.3 nm, are switched by an acousto-optic modulator at a frequency of 6 kHz with an on-off duty cycle of 150 μs on and 17 μs off. The off intervals are needed so that we can introduce pulses of light from the tunable probe laser without having to worry about two-color effects. Based on previous measurements in our system, we estimate the number (3×10^5), density ($5 \times 10^{10} \text{ cm}^{-3}$), and temperature ($\sim 100 \mu\text{K}$) of atoms in the trapped cloud, noting that these are not monitored during our experiments.

We obtain experimental spectra by adding a slow switching sequence to the rapid trap-and-probe modulation. The probe-laser frequency is scanned in a stepwise fashion, with a step size of $\sim 1 \text{ MHz}$ and a stepping rate of $\sim 0.5 \text{ Hz}$. The time spent at each frequency is divided equally between two tasks: the trap is first loaded with Zeeman-decelerated atoms, and then the cloud of atoms is exposed to probe-laser light during the MOT-off intervals. During the trap-loading phase, the deceleration laser beam (tuned 300 MHz below the 811.3-nm transition) propagates through the trapped cloud; meanwhile a mechanical shutter prevents the probe-laser pulses from entering the MOT chamber. After the trap has been loaded for 1 s, both the deceleration laser and the atomic-beam discharge are extinguished. A delay of 10 ms is imposed between this shutoff and the application of probe-laser pulses, ensuring that metastable atoms are no longer entering the observation region during our measurements. Subsequently, the shutter in the probe-laser path is opened, so that UV and ion signals can be accumulated over the course of ~ 2900 cycles of the trap-and-probe modulation. Within each cycle, the probe-laser pulse reaches the atoms 2 μs after the MOT lasers are extinguished and lasts for an exposure time of $\sim 5 \mu\text{s}$.

UV and ion signals are recorded by two multichannel scaler (MCS) units. A solar-blind photomultiplier is used to detect UV photons emitted during the cascading decay of $2p_8$ atoms and/or PLR molecules. The first MCS is gated to count the pulses from this detector only during the probe

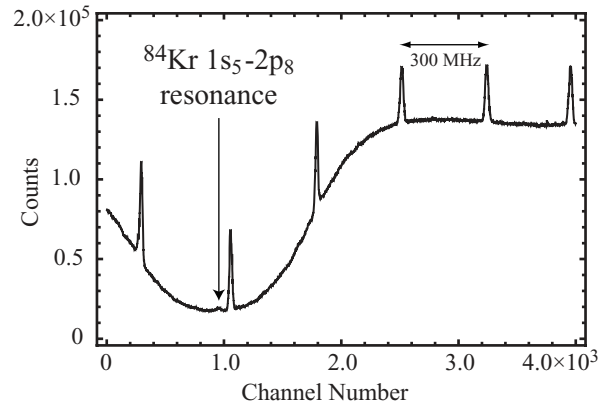


FIG. 4. Combined Fabry-Perot and saturated-absorption signals recorded with a multichannel scaler. The information is used to determine a value of the detuning (Δ) for each step of the probe-laser frequency scan.

exposure. An approximate photon counting efficiency of 10^{-4} is computed from the solid angle subtended by the detector, the UV transmittance of our MgF_2 vacuum window, and the photomultiplier's quantum efficiency. A channel electron multiplier is used to detect ions and to generate the pulses to be counted by the second MCS. We enable this unit to count continuously, thereby recording an ion signal capable of showing laser-induced trap loss. The channel update for each MCS is triggered whenever a probe-laser frequency step is taken. Each channel of the MCS record therefore corresponds to a particular value of Δ .

Scans of the probe-laser frequency are calibrated by way of the transmission signal from a Fabry-Perot interferometer (free spectral range = 300 MHz) and a $1s_5-2p_8$ saturated-absorption signal that we obtain using a dc discharge in a dedicated glass cell. Two laser beams carrying the separate calibration signals are directed onto a single photodiode, and the combined signal is sent through a voltage-to-frequency converter. The resulting pulse rate is recorded by a third MCS, which is synchronized with the photon- and ion-counting MCS units. The recorded data allow us to determine which value of Δ is to be associated with each MCS channel (see Fig. 4). The uncertainty in each value includes a contribution from an estimated $\pm 5 \text{ MHz}$ uncertainty in the zero position for the scan (i.e., the ^{84}Kr atomic resonance). Independent of this, an additional uncertainty of $\pm 1\%$ enters into the relative detuning scale obtained from our fit to the Fabry-Perot signal.

V. PRESENTATION OF DATA

In Fig. 5, we present ion signals obtained over the detuning range $-500 < \Delta < 0 \text{ MHz}$, with a total power of 10 μW in the 1-mm-diameter probe-laser beam. Figure 6 shows the UV signals obtained during the same scans. Single-scan spectra like those displayed in Figs. 5(a) and 6(a) generally have poor signal-to-noise ratios. In principle, one solution to this problem would be to use a longer dwell time for each MCS channel, so as to accumulate more counts at each probe frequency. However, in our setup, as the total time required for a scan approaches 1 hr, a degradation of MOT conditions

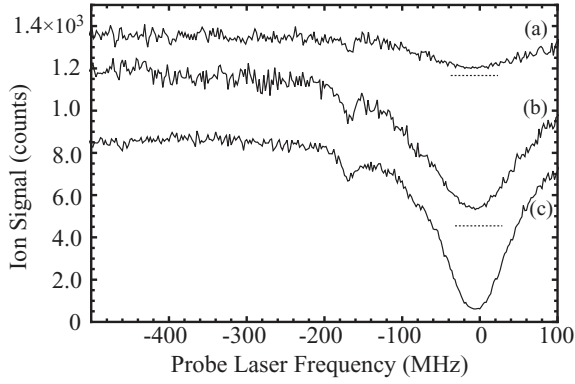


FIG. 5. Ion signals for a probe-laser intensity of $10 \mu\text{W}$: (a) from a single scan of the probe frequency; (b) from the binned average of 17 scans obtained under similar MOT conditions over the course of several consecutive days; (c) as in (b), but for 27 scans obtained over a different series of days. A bin size of 2 MHz is used in (b) and (c). The horizontal dotted lines indicate the zero-level offsets for signals in (a) and (b).

often occurs due to long-term instabilities in the atom-beam discharge and the laser-frequency lock. Considering that we must scan across at least three Fabry-Perot transmission peaks in order to determine the frequency scale, and that we want the probe frequency step size to be ~ 1 MHz for the sake of resolution, we find it reasonable to run scans that cover 1 GHz in about 2000 s. This mode of operation results in a signal-to-noise ratio comparable to that seen in Figs. 5(a)

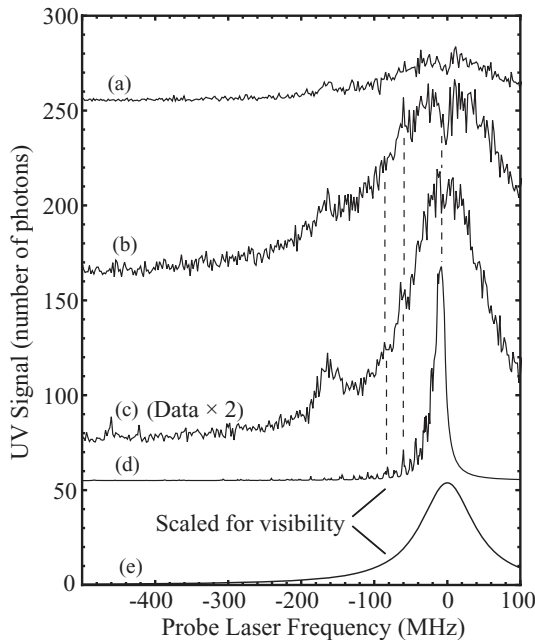


FIG. 6. Graphs (a), (b), and (c) are UV signals obtained following the procedures described for Figs. 5(a)–5(c). (d) Computed molecular UV signal (scaled for visibility) based on the resonances in Fig. 3, approximate Franck-Condon factors obtained as in [7], and a saturation model that accounts for sample depletion. (e) Computed atomic UV signal based on a saturating Lorentzian model that accounts for power broadening and sample depletion. Note that offsets are introduced in graphs (a)–(d) for the sake of presentation.

and 6(a). We have to improve on this ratio by averaging (or summing) the results from multiple scans that are performed under similar conditions.

In order to combine data sets, we must account for the fact that the Δ values assigned to the MCS channels in one probe-laser scan generally do not coincide with those obtained in any other scan. We do this by approximating all detuning values in terms of frequency “bins.” Each bin is assigned an integer bin index (N), and all bins have the same frequency width (ϵ). UV and ion counts from an MCS channel that has an assigned detuning value Δ are put to the bin with approximate detuning $N\epsilon$ if $(N - 1/2) < \Delta/\epsilon \leq (N + 1/2)$. We note that N need not be positive. Since it is the count rate that we wish to measure, the total number of counts that a given scan contributes to a bin must be divided by the number of MCS channels assigned to that bin (or, equivalently, by the total dwell time spent on the bin during that scan). Figures 5(b), 5(c), 6(b), and 6(c) display data that have been binned in this way.

VI. INTERPRETATION OF DATA

In each of our spectra, there is a broad atomic resonance that owes its width to two types of saturation: the familiar form of power broadening and the depletion of atoms in the quenchable sample. The latter effect, which depends on the total time of exposure to the probe laser, dominates the atomic widths seen in Figs. 5 and 6. Saturation of the transition adds a few Γ (at most) to the broadening. The atomic resonance shows up as a fluorescence peak in the UV signal, but since the quenching process removes atoms from the trap (and lowers the cloud density), it produces a broad dip in the ion signal.

An interpretation of other features in our experimental graphs is aided by Figs. 6(d) and 6(e), which show separate theoretical models for molecular and atomic absorption spectra. The vertical scale for each curve is chosen for the sake of presentation; we have not tried to determine how strong the molecular signal should be in relation to the strength of the atomic signal. Our atomic absorption calculation accounts for a finite number of quenchable atoms and for power broadening of the quenching transition. The molecular absorption is obtained from a sum of Lorentzian curves—one for each of the PLR vibrational states. Whereas in Fig. 3 all states contribute with equal weights, in Fig. 6(d) we give each PA transition an approximate probability weight that takes Franck-Condon factors and saturation effects into account. The probability is calculated using the approximations derived in Ref. [7], except that we assume a single, R -independent molecular Rabi frequency for each transition. Thus, the weights do not respect selection rules associated with various combinations of initial and final states, nor do they account for spontaneous linewidths differing from Γ . Also, s -wave collisions are assumed, and there is no provision for rotation in the bound molecular state. Despite these limitations, the computed molecular absorption spectrum does provide a partial set of expected peak positions and a rough picture of where large “clumps” or composite peaks might appear.

The data exhibit a few persistent features within 100 MHz of the atomic resonance that we attribute to single-photon PA into PLR states. The dashed lines in Fig. 6 indicate the alignment of these features with prominent resonances in the model vibrational spectrum of PLR molecules. In both the ion and UV signals, there are small peaks or “shoulders” on the steep part of the atomic scattering curve (roughly at $\Delta = -90$ and -60 MHz). There is also a dip in the UV signal at the top of the atomic resonance; its minimum is consistently found to lie several MHz below $\Delta = 0$. This UV dip has no obvious counterpart in the ion signals shown here, because those signals are already severely weakened by the resonant quenching of atoms.

While the small peaks or shoulders appear to follow the expectations laid out above for the signatures of PLR states (ion dips and UV peaks), the UV dip does not. Nevertheless, it can be interpreted as the result of molecule production in the presence of an optically saturated, quenchable atomic sample. Quenching produces exactly one UV photon per metastable atom. However, for each PLR molecule that is formed, only one atom of the pair is quenched, while the other can gain enough kinetic energy to escape from the trap. If a sample is being quenched rapidly, one can expect a reduction of up to 50% in the per-atom UV emission rate for atoms bound together in PLR states. In light of these considerations, we associate the UV dip near $\Delta = 0$ with the production of PLR molecules that are excited by the probe laser at very large values of R . We find further confirmation of this conclusion when we increase the probe-laser power, so that the atomic transition is strongly saturated and rapid atomic quenching occurs over a range in Δ of several hundred MHz. Under these conditions, the UV features at $\Delta = -90$ and -60 MHz become dips rather than peaks (see Fig. 7). These UV dips can be interpreted as the first one was: they arise when the production of PLR molecules suppresses the per-atom UV rate.

A prominent and relatively broad feature can be seen in Figs. 5 and 6 around $\Delta = -160$ MHz. Its separation from the atomic scattering peak indicates that the system is not subject to rapid quenching in this range of detuning. The observed UV peak and ion dip are therefore consistent with

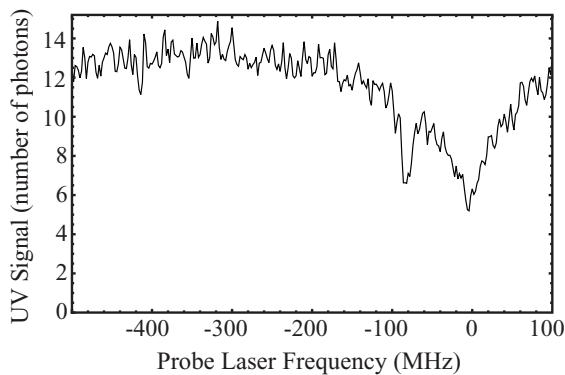


FIG. 7. UV signal obtained with 1 mW of power in the 1-mm-diameter probe-laser beam. The dip at -90 MHz is an inverted version of a peak in Fig. 6. The feature at -60 MHz can also be found to undergo this kind of inversion. By contrast, the feature at -160 MHz in Fig. 6 has no clear counterpart here. An explanation for this intensity dependence is discussed in the text.

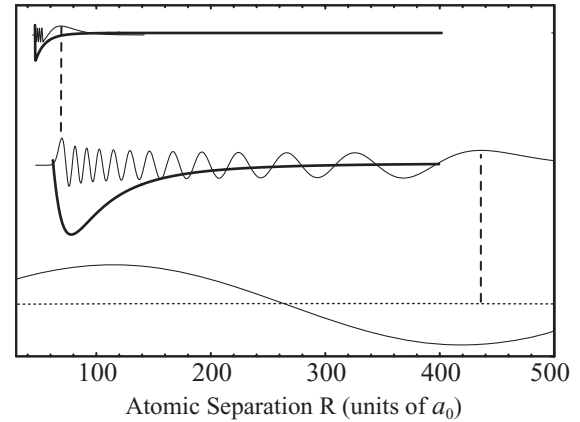


FIG. 8. A scenario for two-step excitation of a doubly excited PLR state. The first step occurs near $450 a_0$ and excites the system from an initial free-atom state to the intermediate, $v = 24$ vibrational state of a PLR potential well with $\Omega = 3$, which lies 160 MHz below the $(1s_5 + 2p_8)$ asymptote. The second step occurs near $70 a_0$ and puts the system in the $v = 7$ state of a well with $\Omega = 4$, lying 320 MHz below the $(2p_8 + 2p_8)$ asymptote. For this double resonance and for several others in the same detuning range, there is a favorable Franck-Condon overlap for the second absorption step.

the expected signature of PLR molecules under conditions of relatively low saturation. We note, however, that the computed, single-photon PA spectrum shows no pronounced resonance (or clump) in this frequency range; nor would the addition of rotational structure to the model result in such a feature. We therefore turn to the possibility of explaining the observed resonance in terms of the excitation of doubly excited PLR states by way of two-photon absorption.

We consider the kind of double excitation illustrated in Fig. 8. After solving for vibrational energies and wave functions in the top ~ 1 GHz of the doubly excited potentials, we find a notable Δ dependence in the probability of two-photon absorption. In particular, over the detuning range of $-200 < \Delta < -120$ MHz, three factors lead to an elevated probability of two-photon PA into PLR vibrational states lying $2|\Delta|$ below the $(2p_8 + 2p_8)$ asymptote. First, there are a number of pairs of singly and doubly excited vibrational states that meet the double-resonance condition in this detuning range, such that $\Delta \approx E_b^{(\text{singly excited})} \approx (1/2)E_b^{(\text{doubly excited})}$. Second, at the small detunings and long distances in question, the Franck-Condon factors for single-photon excitation of the intermediate states can be very large. Finally, in this same range of Δ , the inner turning points of several singly excited states roughly coincide with the outer turning points of certain doubly excited states, and this fact makes for an unusual enhancement in the Franck-Condon factors for the absorption of a second photon. Such enhancement has been discussed previously in the context of single-color excitation of doubly excited, shorter range potentials [8]. What is remarkable in our case is that both the intermediate and the final states are purely long range in character. From this discussion of probability, we can plausibly expect that the signature of doubly excited PLR molecules should be enhanced over a range of detuning around $\Delta = -160$ MHz.

It is also important to consider whether the actual UV and ion signals behave in ways that are fully consistent with the model of double excitation just described. We can do one such consistency check by analyzing data obtained with different levels of probe-laser power. We find that if the power is $1 \mu\text{W}$ or less, no resonance rises above the noise level at $\Delta = -160$ MHz. This result is consistent with the low probability of two-photon transitions in the weak-field limit. If the probe power is raised to 1 mW, then the power-broadened atomic UV signal around $\Delta = -160$ MHz suggests rapid atomic quenching (Fig. 7). There is no resonant depletion in this region that could be attributed to a single-excitation PA process, like the dip at $\Delta = -90$ MHz. There is also no resonant enhancement comparable to what appears at $\Delta = -160$ MHz for a probe power of $10 \mu\text{W}$ (Fig. 6). For high probe intensity, these results are consistent with the scenario in which two-step PA occurs but is indistinguishable from atomic quenching, since these two processes have the same per-atom UV emission rate (one photon per atom).

While this investigation leaves lots of questions open, we judge that the double-excitation model provides the best explanation of what we have seen so far. There is a modest degree of alignment between our calculated single-photon PA peaks and experimental resonances at -90 , -60 , and 0 MHz. This gives us additional confidence that our preliminary observations and modeling of PLR molecules are on the right track. Improvements in our experimental sensitivity and resolution might allow us to measure more peaks, to identify vibrational series, and to test our computations of molecular potentials. Systematic studies of intensity dependence would establish whether particular peaks (and series) should be associated with single or double excitation. If our experiment were modified to allow for both higher atomic density and initial-state selectivity, perhaps through the use of a magnetic trap or a far-off-resonant (dipole-force) laser trap, we would be able to perform targeted studies of particular transitions and final states. Our plan is to develop such capabilities and to build significantly on the initial exploration described here.

ACKNOWLEDGMENTS

This work has been supported by Calvin College and by a grant from the National Science Foundation (PHY-0554807).

APPENDIX

Our calculations involve more atomic states than are shown in Fig. 1. We start with a large basis containing 27 atomic states

TABLE I. Atomic states that are included as elements of the algebraic basis for computations of molecular potentials. The states shown in Fig. 1 are also included. The truncated basis mentioned in the Appendix is composed of the states in Fig. 1 and the three states indicated here in bold.

Paschen notation	Pair-coupling notation	Energy (cm^{-1})
$1s_3$	$5s' [1/2]_0$	85191.6166
$1s_2$	$5s' [1/2]_1$	85846.7046
$2p_{10}$	$5p [1/2]_1$	91168.5150
$2p_7$	$5p [3/2]_1$	92964.3943
$2p_6$	$5p [3/2]_2$	93123.3409
$2p_5$	$5p [1/2]_0$	94092.8626
$2p_4$	$5p' [3/2]_1$	97595.9153
$2p_3$	$5p' [1/2]_1$	97919.1468
$2p_2$	$5p' [3/2]_2$	97945.1664
$2p_1$	$5p' [1/2]_0$	98855.0698
$3d_1''$	$4d [5/2]_2$	98867.429
$3d_1'$	$4d [5/2]_3$	99079.367
$4d_3$	$5d [3/2]_2$	105007.245
$2s_3$	$6s [1/2]_0$	105091.35
$2s_2$	$6s [1/2]_1$	105146.33
$4d_1''$	$5d [5/2]_2$	105163.499
$4d_1'$	$5d [5/2]_3$	105208.476
$3s_5$	$7s [3/2]_2$	105647.4536
$4d_2$	$5d [3/2]_1$	105648.434
$3s_4$	$7s [3/2]_1$	105770.7014

that either are involved in (nearly) resonant electric dipole couplings or are fed by spontaneous decay when the system is exposed to 811-nm laser light (Table I). We run tests to find out which of these states can be eliminated without significantly affecting the PLR potential wells. For the purposes of this paper, we use just ten atomic states, with the basis truncation introducing at most a $\sim 1\%$ error in the singly excited potentials (and a few times this error in the doubly excited potentials). Note that because of Zeeman degeneracy, each atomic state contributes $(2J + 1)$ basis states to the computation.

In Table I, energies (cm^{-1}) are from the NIST Atomic Database [9]. Our calculations use values for $2p \rightarrow 1s$ transition rates (A_{ki}) that can be found in [4]. The $4d_4' \rightarrow 2p_9$ transition rate is taken from [10]. Rates for other (downward) transitions into the $2p$ states are estimated from line intensities listed in [9]. In converting energy units, we assume $1 \text{ cm}^{-1} = 29.979 245 8 \text{ GHz}$.

- [1] M. R. Doery, E. J. D. Vredendregt, J. G. C. Tempelaars, H. C. W. Beijerinck, and B. J. Verhaar, *Phys. Rev. A* **57**, 3603 (1998).
 [2] J. Lefers, N. Miller, D. Rupke, D. Tong, and M. Walhout, *Phys. Rev. A* **66**, 012507 (2002).
 [3] W. C. Stwalley, Y.-H. Uang, G. Pichler, *Phys. Rev. Lett.* **41**, 1164 (1978); K. M. Jones, E. Tiesinga, P. D. Lett, and P. S. Julienne, *Rev. Mod. Phys.* **78**, 483 (2006); J. Weiner, *Cold and*

Ultracold Collisions in Quantum Microscopic and Mesoscopic Systems (Cambridge University Press, Cambridge, England, 2003).

- [4] K. Dzierzega, U. Volz, G. Nave, and U. Griesmann, *Phys. Rev. A* **62**, 022505 (2000).
 [5] F. Pereira Dos Santos, F. Perales, J. Léonard, A. Sinatra, Junmin Wang, F. Saverio Pavone, E. Rasel, C. S. Unnikrishnan, and

- M. Leduc, *Eur. Phys. J. D* **14**, 15 (2001); F. Shimizu, K. Shimizu, and H. Takuma, *Phys. Rev. A* **39**, 2758 (1989); H. Katori and F. Shimizu, *Phys. Rev. Lett.* **73**, 2555 (1994); M. Walhout, U. Sterr, C. Orzel, M. Hoogerland, and S. L. Rolston, *ibid.* **74**, 506 (1995).
- [6] J. W. Cooley, *Math. Comput.* **15**, 363 (1961).
- [7] P. S. Julienne, *J. Res. Natl. Inst. Stand. Technol.* **101**, 487 (1996).
- [8] A. Amelink, K. M. Jones, P. D. Lett, P. van der Straten, and H. G. M. Heideman, *Phys. Rev. A* **62**, 013408 (2000).
- [9] Yu. Ralchenko, A. E. Kramida, and J. Reader (NIST ASD Team), NIST Atomic Spectra Database (version 3.1.5), National Institute of Standards and Technology, Gaithersburg, MD. Available at <http://physics.nist.gov/asd3>.
- [10] B. D. Cannon, W. L. Glab, and R. Ogorzalek-Loo, *Phys. Rev. A* **47**, 147 (1993).